Scientific Reports

https://doi.org/10.1038/s41598-026-41757-z

Article in Press

A non-intrusive framework using acoustic signals and deep learning for boiling diagnostics in visual-limited environments

Received: 23 December 2025

Accepted: 23 February 2026

Published online: 25 March 2026

Cite this article as: Huang P., Seong J.H., Castro-Aguilar J.M. *et al.* A non-intrusive framework using acoustic signals and deep learning for boiling diagnostics in visual-limited environments. *Sci Rep* (2026). https://doi.org/10.1038/s41598-026-41757-z

Pei-Hsun Huang, Jee Hyun Seong, Jonathan Mario Castro-Aguilar, Christiaan Vermeulen & Ellen Margaret O'Brien

A Non-Intrusive Framework Using Acoustic Signals and Deep Learning for Boiling Diagnostics in Visual-Limited Environments

Pei-Hsun Huang[a], Jee Hyun Seong[b], Jonathan Mario Castro-Aguilar[a], Christiaan Vermeulen[a], and Ellen Margaret O'Brien[a*]

[a]Los Alamos National Laboratory,
P.O. Box 1663, Los Alamos, NM, 87545, USA
[b]Korea Advanced Institute of Science & Technology,
291 Daehak-ro, Yuseong District, Daejeon, 34141, Republic of Korea
*emobrien@lanl.gov

Abstract

Accurate monitoring of boiling heat transfer is critical for safeguarding high-power systems operating in environments where conventional optical diagnostics are hindered by radiation fields or restricted visual accessibility. This study presents a non-intrusive framework that integrates hydroacoustic sensing with deep learning to infer near-wall boiling characteristics and enable predictive thermal assessment without visual access. In a prototypical subcooled flow-boiling facility representative of the Isotope Production Facility (IPF) at Los Alamos, hydrophones capture boiling-induced acoustic emissions that are transformed into background-removed Short-Time Fourier Transform (STFT) spectrograms. A convolutional neural network (CNN) then regresses heat flux, wall superheat, and key bubble parameters directly from these spectrograms. The CNN achieved predictive accuracy under nominal conditions and demonstrated robustness and generalization under acoustic noise for Signal-to-Noise Ratios (SNRs) down to approximately 0 dB. When integrated into an ANSYS CFX wall-boiling model, the acoustically inferred parameters reproduced boiling curve and critical heat flux (CHF) values consistent with image-based

benchmarks. Furthermore, the model retained reliable performance under moderate variations in bulk temperature, flow rate, and hydrophone placement, confirming its generalizability across practical boundary conditions. These results demonstrate the feasibility of hydroacoustic-based deep learning as a viable path toward real-time, radiation-tolerant boiling diagnostics and predictive thermal safety assessment in inaccessible systems such as the IPF.

KEYWORDS:

Subcooled flow boiling, Boiling acoustics, Machine learning, Critical heat flux, CFD

1. Introduction

Accurate evaluation of boiling heat transfer is critical for the safe and efficient operation of high-power thermal systems, especially in radiation-intensive environments such as nuclear reactors and particle accelerators. In such settings, conventional experimental diagnostics are severely constrained due to radiation-induced limitations on instrumentation. One embodied challenging case is the Isotope Production Facility (IPF) at the Los Alamos Neutron Science Center (LANSCE), where a 100 MeV proton beam irradiates stacked, encapsulated targets for medical and scientific isotope production [1]. During operation, subcooled water is used to extract heat from the target stack. At high beam currents, the intense surface heat flux can induce near-wall nucleate boiling. If the heat flux exceeds a critical threshold, this may escalate to a critical heat flux (CHF) condition – a boiling crisis that can compromise the structural integrity of the target. Predicting boiling heat transfer in such systems typically relies on Computational Fluid Dynamics

(CFD) models, which require accurate input parameters characterizing vapor bubble behavior near heated surfaces. Given that in-situ visualization is not feasible in such an intense radiation environment, our previous works have developed experimental-computational frameworks using a prototypical experimental facility and provide surrogate data for CFD validation [2]. However, further enhancement through non-invasive diagnostic tools – specifically those that can be implemented at IPF – remains essential for reliably capturing the underlying boiling dynamics in this radiation-constrained environment.

Hydroacoustic sensing has emerged as a promising solution. Hydrophones can detect acoustic emissions generated during boiling and have been successfully deployed in radiation environments [3], [4]. In our previous work, distinct acoustic signatures corresponding to different boiling regimes were identified using Fast Fourier Transform (FFT), Short-Time Fourier Transform (STFT), and spectral entropy analysis [5]. Independent studies have further demonstrated that acoustic signals can be used to detect the onset of a boiling crisis [6] – [9]. In addition to CHF detection, prior research has also established correlations between acoustic features – such as frequency content and sound pressure level (SPL) – and key boiling parameters, including heat flux [10], [11], wall superheat [10], [12], nucleation site density [10], and bubble diameter [13], [14]. However, the majority of the studies focus on pool boiling and the derived empirical relationships lack generalizability across different flow and boundary conditions [12], [15], [16].

Given these limitations, machine learning (ML) approaches – particularly Convolutional Neural Networks (CNNs), which excel at extracting complex features from image data – offer a promising direction for advancing boiling analysis. In our previous work, U-Net CNN architecture was employed to segment boiling bubbles

in high-speed video (HSV) imagery [2]. Other studies have shown success in real-time prediction of bubble characteristics using feedforward neural networks [19], and in classifying heat flux regimes based on learned visual patterns [20]. The successes of these image-based ML approaches have paved the way for applying such techniques to boiling acoustics.

Hydroacoustic signals can be transformed into time-frequency representations such as spectrograms, which preserve temporal features and can be processed as image-like inputs for ML. This allows image-based CNN architectures to be effectively applied to acoustic data. Several studies have linked acoustic features to boiling regimes using visual ground truth, enabling classification of pool [21] – [24] and flow boiling [25] systems. ML models have also shown potential in detecting CHF conditions [22], [23] and estimating heat flux [26], [27] and heat transfer coefficient [27] via regression on spectral features. While prior studies have demonstrated acoustic-based boiling regime identification, CHF detection, or regression of individual thermal quantities, they have not shown how acoustically inferred information can be translated into physically meaningful bubble-scale inputs required by CFD heat-partitioning models.

To address this challenge, our preliminary study demonstrated the feasibility of a CNN model to predict bubble parameters from background removed-STFT spectrograms in the prototypical TARDIS-β facility [28]. Building upon these findings – as well as our earlier work on visual [2] and acoustic [5] analysis – we further enhanced the framework's capability to predict heat flux and wall superheat. The improved model was evaluated for its resilience under varying acoustic noise levels, integrated within the ANSYS CFD wall-boiling framework, and tested for generalizability across a wide range of operating conditions. This study

demonstrates the feasibility of a non-intrusive, acoustics-driven pathway for informing CFD-based boiling analysis in visually restricted environments, with particular relevance to radiation-limited systems such as the IPF.

2. Methodology

The present study integrates HSV visual data, predictive CFD models using ANSYS CFX [29], boiling acoustic signals, and machine learning techniques into a unified diagnostic framework, as illustrated in Figure 1. By correlating boiling acoustic emissions with experimental parameters – such as wall superheat, heat flux, and boiling bubble characteristics – our goal is to develop a predictive CFD model that relies solely on machine learning models trained on hydrophone input. This approach lays the groundwork for future implementation of AI/ML techniques coupled with hydroacoustic diagnostics at the IPF, where conventional visualization techniques are not feasible.

This section is structured as follows: Section 2.1 provides an overview of the IPF cooling system and the TARDIS-β prototypical test facility, along with descriptions of data reduction procedures and uncertainty quantification. Section 2.2 and 2.3 describe the architecture and implementation of the deep learning model and the predictive CFD model, respectively.

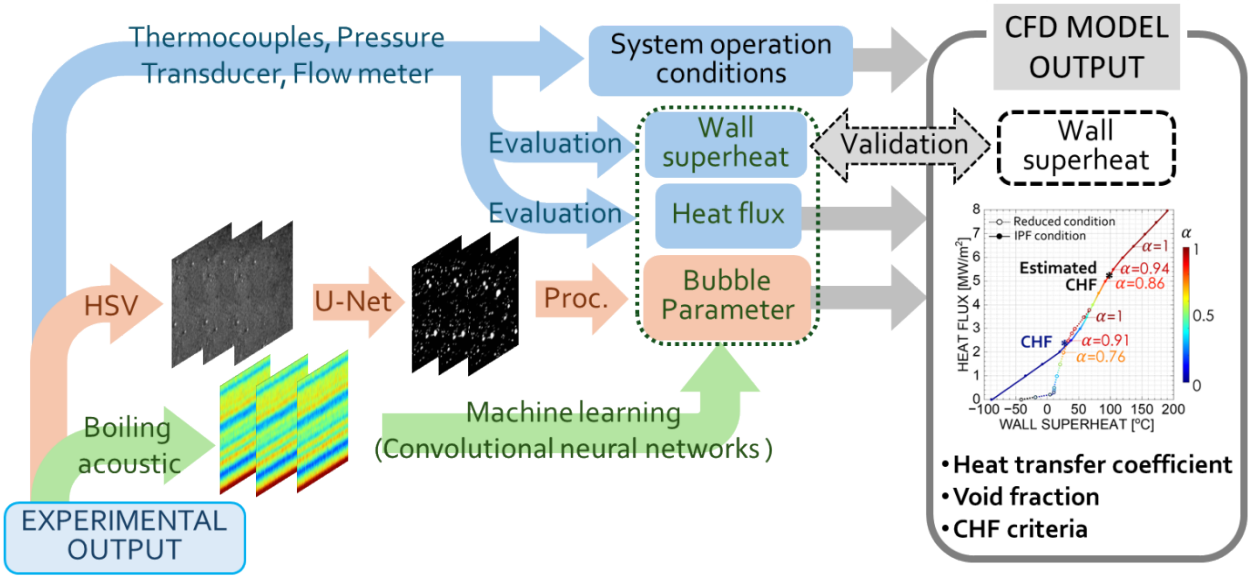

Figure 1 Experimental and computational framework to predict subcooled flow boiling.

2.1 Experimental Setup

2.1.1 IPF targets stack station

As illustrated in Figure 2 (a), the targets stack station at IPF is located beneath a 12.2 m (40 ft) water column and irradiated by a 100 MeV proton beam. At this depth, the static pressure is approximately 200 kPa, accounting for the facility's elevation of 2,500 m above sea level. Figure 2 (b) shows a schematic of the targets stack station's cooling system. Under high beam currents, subcooled flow boiling occurs near the beam-facing surfaces, which comprise the window and three encapsulated targets, all fabricated from nickel-625. Deionized (DI) water at approximately 35°C is circulated beneath the targets stack at a total flow rate of 8,996 kg/m^2/s (equivalent to 40 GPM). The flow is assumed to be evenly distributed across four subchannels – formed by the gaps between the window and the encapsulated targets – each receiving approximately 2,249 kg/m^2/s (10 GPM). After passing through the

subchannels, the coolant converges and exits through an annular discharge channel around the targets station. This flow configuration allows the proton beams to irradiate the encapsulated targets situated within the central region.

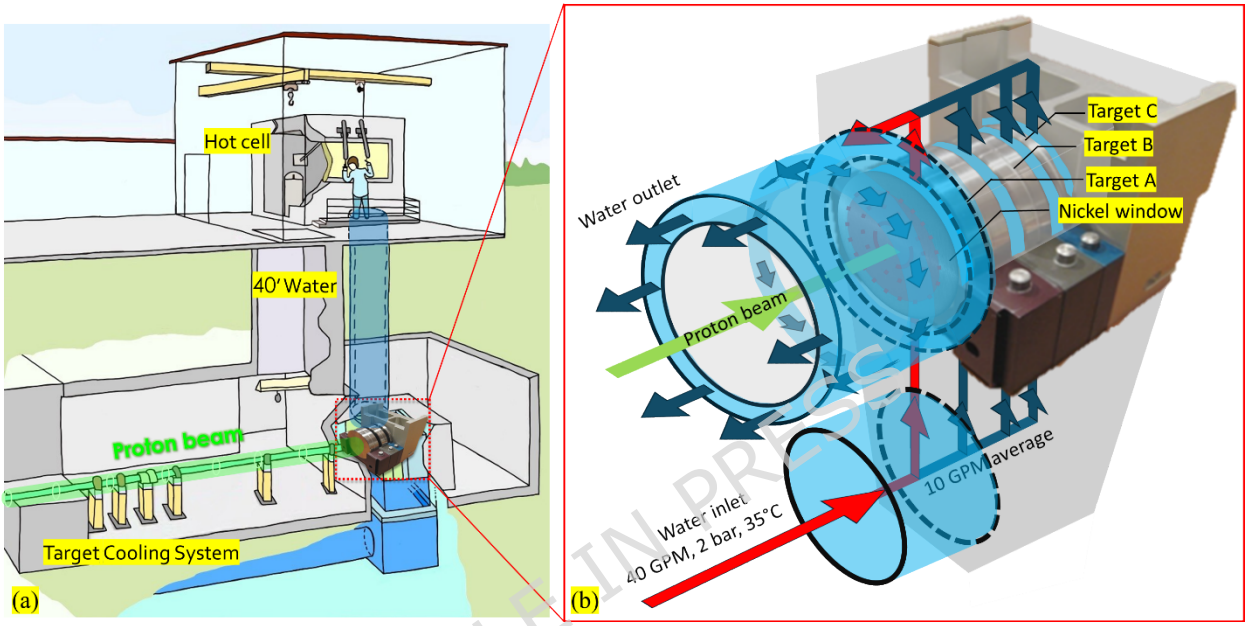

Figure 2 (a) IPF schematics; (b) Targets stack station cooling configuration.

2.1.2 TARDIS-β test facility

The prototypical TARDIS-β facility was developed to replicate a single cooling-water subchannel in the IPF target stack station (indicated by red arrows in Figure 2 (b)). A schematic of the flow loop and instrumentation layout is shown in Figure 3. The flow loop is filled with deionized (DI) water and pressurized to 200 kPa (29 psi) using argon gas. System pressure is monitored via both pressure gauge and OMEGA pressure transducers (PTs), while bulk water temperature is monitored by an

ungrounded K-type thermocouple (TC). The flow rate is continuously tracked using a clamp-on digital flow sensor (FD-Q32C).

The TARDIS-β facility is equipped with a high-speed video (HSV) camera system (DANTEC DYNAMICS - SpeedSense VEO), paired with a Nikon Telephoto AF Micro Nikkor 200mm f/4.0D ED-IF lens, providing an image resolution of 20 μm/pixel. A transparent plexiglass window in the test section enables optical access to the two-phase flow within the 5.5 × 51 mm^2 rectangular channel. To capture boiling-induced acoustic emissions, the system is instrumented with a pair of hydrophones (RESON TC4013-1), each connected to a VP-2000 voltage preamplifier (RESON EC6081 MK2). Hydrophone mounting ports are positioned at various distances (6, 22.5, 39, and 55.5-inches) from the test section window, enabling assessment of the influence of sensor placement on the recorded acoustic signals. Acoustic signals are acquired via a National Instruments (NI) VirtualBench™ system. Additional measurements – including temperatures, pressures, and flow sensor outputs – are collected using NI CompactRIO modules and synchronized and recorded through a LabVIEW-based data acquisition interface.

In the test section, volumetric heating is applied to a 30 mm diameter, 5 mm thick nickel-625 disk using a 20 kW GH Induction Atmosphere induction heating system equipped with a 30 mm pancake coil. A pair of ungrounded K-type thermocouples (OMEGA) are embedded within the disk, allowing estimation of heat flux and wall superheat. The bulk water temperature is controlled by adjusting the induction heater power output and the setpoint of the external chiller system.

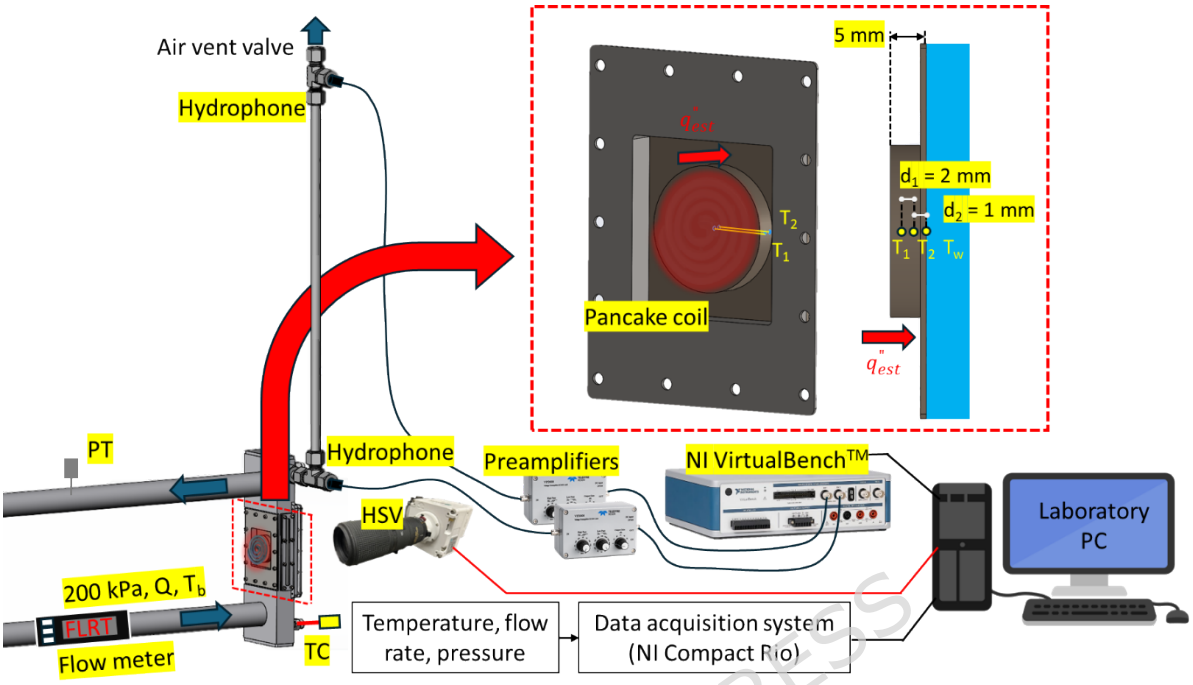

Figure 3 TARDIS-β element diagram and thermocouple arrangement in the nickel test section.

2.1.3 Data Reduction

As illustrated in Figure 3, the heat flux applied to the test section (q''_{est}) and the boiling wall temperature (T_w) were calculated using a one-dimensional conductive heat transfer equation from a pair of thermocouples embedded within the heated disk:

$$q''_{est} = \frac{k_{12}(T_1 - T_2)}{d_1} = \frac{k_{2w}(T_2 - T_w)}{d_2} \quad (1)$$

Here, k_{12} and k_{2w} are the thermal conductivity of nickel-625 at the temperature of $(T_1+T_2)/2$ and $(T_2+T_w)/2$, respectively. The thermal conductivity of nickel-625 is temperature dependent and can be expressed as follows [35]:

$$k(T) = 6.515 \times 10^{-5}T^2 + 0.01432T + 9.514 \text{ [W/m/K]} \quad (2)$$

The uncertainty in the calculated heat flux ($U_{q''_{est}}$) and wall temperature (U_{T_w}) were evaluated using error propagation analysis. A 3% error was assigned to thermocouple readings (i.e., T_1, T_2), and the standard deviation from 20 s steady-state temperature measurements (U_{std}) was incorporated. In addition, a ±22% variation – applied to both $U_{q''_{est}}$ and U_{T_w} – was included to account for fluctuations in heating performance observed at identical induction heater power settings (U_{flu}) (Figure 4). Using Eq. (3) and (4), a ±25% uncertainty was applied for both $U_{q''_{est}}$ and U_{T_w}.

$$U_{q''_{est}}^2 = \left(\frac{T_2 - T_1}{d_1}\right)^2 U_{k_{12}}^2 + \left(\frac{k_{12}}{d_1}\right)^2 U_{T_1}^2 + \left(\frac{k_{12}}{d_1}\right)^2 U_{T_2}^2 + U_{std}^2 + U_{flu}^2 \quad (3)$$

$$U_{T_w}^2 = U_{T_2}^2 + \left(\frac{d_2}{k_{2w}}\right)^2 U_{q''_{est}}^2 + \left(\frac{q''_{est} d_2}{k_{2w}^2}\right)^2 U_{k_{2w}}^2 + U_{std}^2 + U_{flu}^2 \quad (4)$$

Boiling parameters were extracted from image sequences recorded by the HSV camera using previously developed algorithms [34]. These parameters including bubble departure diameter (D_d), departure frequency (f), wait time (t_w), and nucleation site density (N''). A range in D_d, f, and t_w were quantified based on standard deviations over 4,000 frames (acquired at 24,000 fps). The statistical range ($U\phi$) for each parameter (ϕ) was estimated using the following relation [36]:

$$U\phi^2 = \frac{1}{\sum_{s=1}^{N_s} N_{b,s}} \sum_{s=1}^{N_s} \sum_{n_{b,s}=1}^{N_{b,s}} \left(\phi_{n_{b,s}} - \overline{\phi}\right)^2 \quad (5)$$

where N_s is the number of nucleation sites, $N_{b,s}$ is the number of bubble events observed at the s^{th} nucleation sites.

To estimate the range in nucleation site density N'', the image frame (with a resolution of 512 × 512 pixels^2) was subdivided into subregions of 8 × 8 pixels^2. The standard deviation of N'' was then computed across these subregions for each measurement sequence.

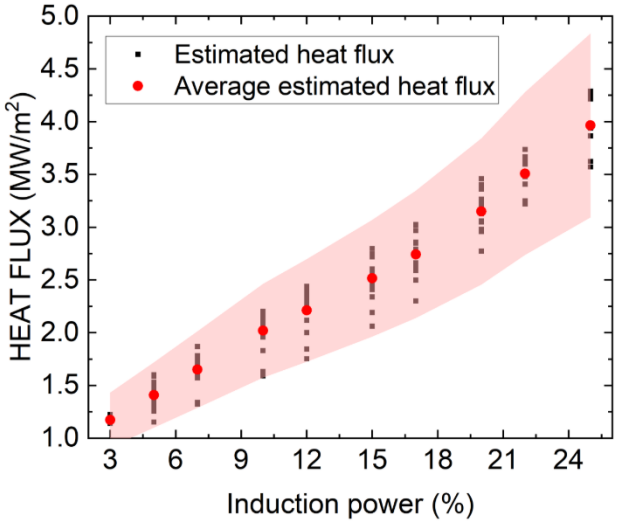

Figure 4 Variation of estimated heat flux with induction heating power. The shaded region denotes a ±22% deviation from the mean value at each power level.

2.2 Deep Learning Models

Convolutional Neural Networks (CNNs) represent a class of deep learning architectures that are particularly effective for processing structured, grid-like data such as images. These models have been widely adopted across various domains for both feature extraction and regression tasks due to their capacity to learn hierarchical representations. In this study, we employed two CNN-based architectures: (1) a U-Net CNN model for segmentation of boiling bubbles in high-speed video (HSV) data, and (2) a regression CNN model to correlate boiling acoustic emissions with fundamental boiling parameters.

2.2.1 Image processing

In prior work [2, 30], HSV images were successfully processed using a U-Net-based transfer learning framework to segregate boiling bubbles. Key bubble parameters

were extracted using custom-developed image processing algorithms. These parameters were then used as inputs to the heat partitioning equations in the CFD model to predict bubble dynamics and improve thermal simulations.

In the present study, additional preprocessing steps were introduced to enhance the robustness of image processing. Background noise was minimized by employing cross-correlation techniques to identify and correct slight spatial misalignments between the background and raw HSV image frames. Such displacements can result from mechanical vibrations in the HSV camera or the test facility during operation. Furthermore, a power calibration procedure was integrated into the image processing workflow to compensate for frame-to-frame intensity fluctuations. These variations are primarily caused by high-frequency oscillations in the flash illumination received by the HSV camera, which can impair the consistency of bubble segmentation. The implemented correction algorithm standardizes image brightness across the entire sequence, thereby improving the accuracy and reliability of the extracted bubble parameters. Figure 5 illustrates the schematic overview of the complete image processing workflow, including the preprocessing, segmentation, calibration, and parameter extraction steps.

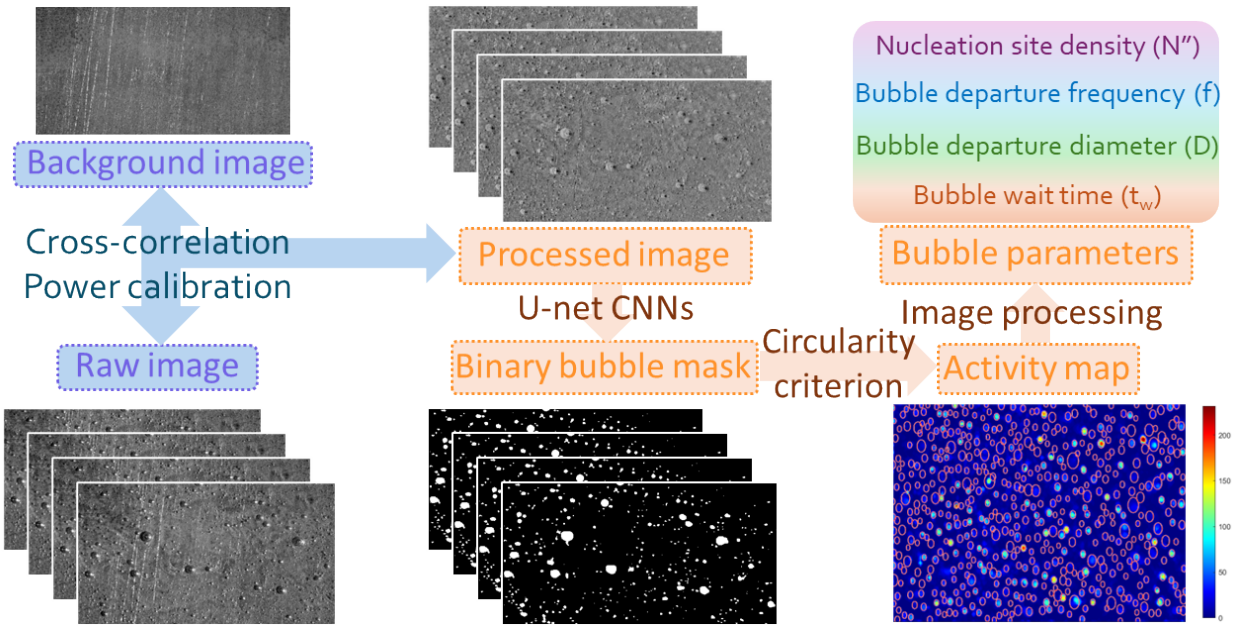

Figure 5 Workflow of image segregation using U-net CNNs.

2.2.2 Acoustic signal regression

To predict key boiling parameters extracted from HSV imagery using acoustic signals, an image-based regression model was developed. The schematic of the CNNs model architecture and workflow is illustrated in Figure 6. Prior to being fed into the model, raw acoustic signals were converted into time-resolved frequency spectra using a Short-Time Fourier Transform (STFT). The frequency range of 0 - 5 kHz was selected as the region of interest for capturing boiling-related acoustic signals based on our observation and literature [6]. To reduce background noise – particularly prominent under high flow rate conditions – the resulting spectra were further processed by subtracting averaged background STFT obtained under non-boiling conditions, as validated in our previous work [5]. This preprocessing step enhances signal clarity by isolating boiling-induced acoustic features. The spectra were then segmented into 0.1 s averages over a 21 s hydrophone recording

(sampling rate of 100 kHz), yielding 202 samples for each operating condition. The resulting spectrograms were formatted as grayscale images for CNN-based feature extraction and regression learning.

The regression model was implemented using the Keras Functional API [38]. The network accepts preprocessed spectrograms in the form of 224 × 224 × 1 grayscale images as input and maps them to continuous-valued heat flux, wall superheat, and boiling parameters through a sequence of convolutional and fully connected layers. The acoustic spectrogram dataset was randomly partitioned at the sample level into disjoint training and test subsets using a fixed random seed to ensure reproducibility. The data were divided into 70% and 30% for model training and validation, respectively. A hold-out validation strategy was employed because the regression targets represent continuous physical quantities and the intended application focuses on generalization to new measurements acquired under known operating conditions. Given the high dimensionality of the CNNs, repeated retraining under cross-validation was not pursued.

Feature extraction was achieved through a sequence of six convolutional blocks with progressively increasing filter counts (32, 64, 128, 128, 128, 256). Each block applied a 3 × 3 convolution with unit stride and same padding, followed by a squeeze-and-excitation (SE) module to adaptively recalibrate channel responses. Batch normalization was applied after each convolution to stabilize training, while the Swish activation function introduced non-linearity with smooth gradient properties. A 2 × 2 max-pooling layer in each block reduced spatial resolution while preserving salient features. After the final convolutional stage, feature maps were condensed using global max pooling, which aggregated information across the entire spatiotemporal domain without the need for explicit flattening. The pooled

representation was passed to a fully connected projection layer with 512 hidden units. To enhance generalization, an L_2 weight penalty ($\lambda = 0.005$) was applied to this layer. The projection was further stabilized using layer normalization and Swish activation.

The regression head produced six continuous outputs corresponding to the heat flux, wall superheat, and boiling parameters of interest. Model training employed the Adam optimizer with a learning rate of 1×10^{-4}. To account for heteroscedasticity in the experimental data, a weighted mean squared error (WMSE) loss function was used, where the weight assigned to each training example is the inverse of the associated measurement range (uncertainty bar) derived from Section 2.1.3. This strategy ensures that predictions are guided more strongly by reliable labels, while reducing sensitivity to noisy measurements. The number of training epochs is adaptively determined to achieve a fixed total number of gradient update iterations, computed as:

$$\text{EPOCHS} = \frac{\text{total iterations}}{\text{steps per epoch}}$$

Model training was performed for a total of 80,000 iterations with early stopping based on validation loss. Additional evaluation of model stability and generalization, including learning curve analysis, ablation studies, and comparisons with baseline models, is presented in subsequent sections.

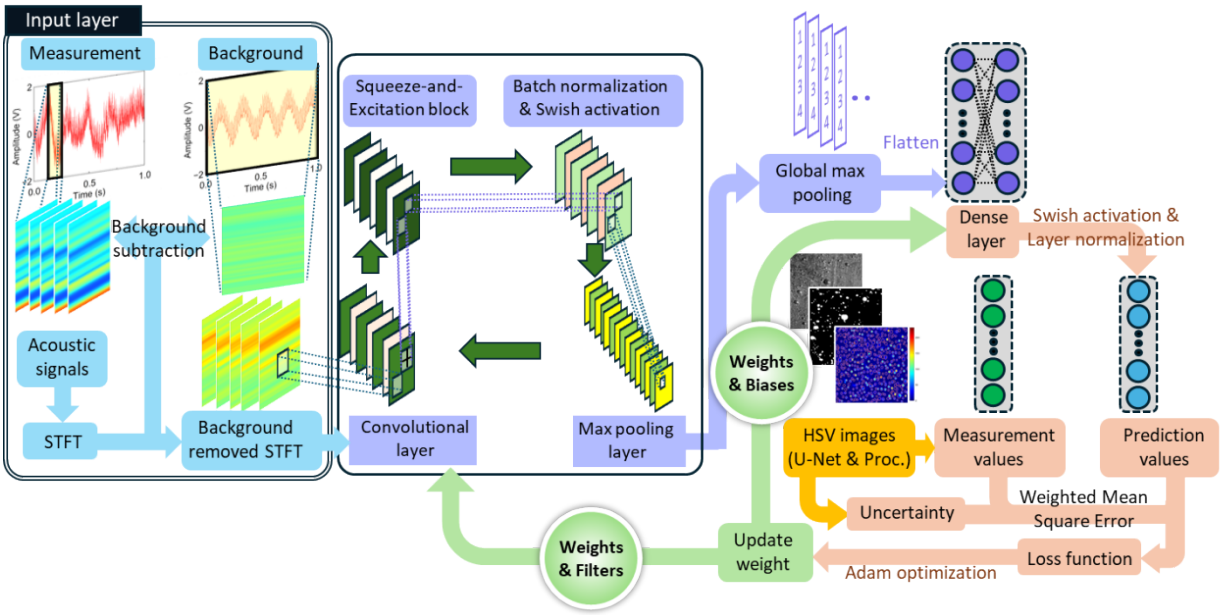

Figure 6 Schematic of the image-based regression CNN trained on boiling acoustic emission

2.3 CFD Model

In our previous work, CFD models were developed using ANSYS CFX to simulate subcooled flow boiling in both the TARDIS-β experimental facility and the IPF cooling system [2]. The simulations employed the Rensselaer Polytechnic Institute (RPI) wall boiling model to resolve the near-wall two-phase heat transfer behavior. The RPI model is based on a heat partitioning approach, in which the total wall heat flux is divided into three components: evaporation heat flux (q''_e), quenching heat flux (q''_q), and single-phase convection heat flux (q''_c). These are defined by the following equations:

$$q''_e = fN'' \frac{\pi}{6} D^3 \rho_v h_{lv} \tag{6}$$

$$q''_q = fN'' K \frac{\pi}{4} D^2 2\varepsilon_l \sqrt{\frac{t_w}{\pi}} (T_w - T_b) \tag{7}$$

$$q''_c = \left(1 - N'' K \frac{\pi}{4} D^2\right) h_c (T_w - T_b) \tag{8}$$

In the above equations, ρ_v is vapor density, h_{lv} is latent heat of vaporization, ε_l is effusivity of liquid water, h_c is single-phase convection heat transfer coefficient, and K is area influence factor. Among these, ρ_v, h_{lv}, and ε_l are fundamental thermal properties. K is the area influence factor, typically 4, assuming a departing bubble affects a region twice its diameter [37]. The convection heat transfer coefficient h_c can be estimated using well-established empirical correlations under known flow conditions.

Within the RPI heat-partitioning framework implemented in ANSYS CFX, the single-phase convective heat transfer coefficient is calculated using standard turbulent convection closures, while the evaporative and quenching heat flux components are evaluated using experimentally measured bubble parameters; interfacial heat transfer is modeled using the Ranz-Marshall correlation for the liquid phase with zero thermal resistance assumed for the vapor phase, following the framework previously validated against independent experimental boiling curves and CHF measurements [2]. The overall accuracy of the CFD model is primarily governed by the fidelity of the input bubble parameters – specifically, N'', D, f, and t_w. As shown in the workflow in Figure 5, these parameters are extracted from HSV imagery using

image-processing algorithms or, in the present study, inferred directly from boiling acoustic signals using a trained CNN-based regression model.

In the present study, the CFD model is employed as a physics-based consistency framework to examine whether boiling parameters inferred from hydroacoustic signals can serve as physically meaningful inputs to a mechanistic wall-boiling model, rather than as an independently validated CHF predictor. CFD simulations were performed using bubble parameters derived from HSV imagery and, separately, using parameters predicted by the CNN model from acoustic data. The resulting boiling curves and CHF trends were compared to assess internal physical consistency between the two parameter sources. Consistent with the engineering criterion adopted in our previous work [2], CHF is defined in the CFD framework as the condition at which the local void fraction reaches 0.9. This formulation enables a quantitative, physics-consistent comparison of acoustically inferred and visually derived boiling inputs within an established wall-boiling framework.

3. Results and Discussion

This section presents a comprehensive evaluation of the CNN-based model's predictive performance across a range of operating and boundary conditions. Following model development, the CNN models were first evaluated, trained, and validated using datasets collected under identical experimental settings with progressively increasing heat fluxes to establish baseline accuracy. All reported prediction errors and comparisons in this section are computed exclusively on the held-out test dataset, which was not used during model training. To assess resilience against acoustic contamination, controlled levels of artificial white noise were

superimposed onto the recorded signals. The bubble parameters inferred from the CNN were then incorporated into the CFD framework to simulate the corresponding boiling curves and predict the CHF. These results were quantitatively compared against reference values derived from HSV imagery and thermocouple (TC) measurements to evaluate physical consistency. Finally, the influence of key operational parameters – including bulk temperature, flow rate, and hydrophone placement – was systematically examined to assess the model's robustness and generalizability beyond the training conditions.

3.1 Model Evaluation and Prediction

In this section, the performance of the proposed CNN is first evaluated through learning curve analysis, comparisons with simpler baseline models, and systematic ablation studies to assess overfitting, architectural necessity, and generalization behavior. Then, the validated model is applied to predict boiling heat transfer characteristics under representative operating conditions, and the results are compared against reference measurements. The IPF and Intermediate conditions are used for model evaluation, while the IPF and Reduced conditions are used to demonstrate model prediction capability. The corresponding operating parameters and acoustic sampling numbers are summarized in Table 1.

Table 1 . Experiment conditions and acoustic spectrum sampling number for each case.

Name	Bulk temperature (T_b)	Flow rate (Q)	Heat flux (q''_{est})	Sampling number

IPF condition	35°C	10 GPM	2.1 – 5 MW/m^2 (5 conditions)	1,010
Intermediate condition	55°C	7, 10 GPM	1.3 – 5.1 MW/m^2 (34 conditions)	6,868
Reduced condition	60°C	1.5 GPM	1 – 2.4 MW/m^2 (5 conditions)	1,010

3.1.1 Model evaluation

To evaluate the training behavior and guard against overfitting, Figure 7 presents the training and validation loss histories for the CNN under the IPF condition. The learning curves exhibit closely coupled convergence without late-epoch divergence, indicating stable optimization and limited overfitting.

To assess whether the predictive performance arises from the proposed architecture rather than unnecessary model complexity, the CNN was benchmarked against simpler baseline models and evaluated through targeted ablation studies. The baselines include linear regression and a multilayer perceptron (mlp) operating on flattened spectrogram inputs, while ablated CNN variants were constructed by reducing network depth, replacing the Swish activation with ReLU, or shrinking the final dense layer. Model performance was quantified using the normalized root-mean-square error (NRMSE), calculated as:

$$\mathrm{NRMSE} = \frac{\sqrt{\frac{1}{n}\sum_{i=1}^{n}\left(y_i^{pred} - y_i^{true}\right)^2}}{\sigma_y} \tag{9}$$

where n is sample number, and σ_Y denotes the standard deviation of the ground-truth labels. A NRMSE value below unity (< 1) was considered indicative of acceptable model performance, corresponding to deviations within the experimental uncertainty of reference data.

Figure 8 summarizes the NRMSE results for the IPF condition. Reducing the convolutional depth to three blocks, shrinking the dense layer, or replacing the activation function to ReLU consistently degrades performance across regression targets, indicating that the selected architectural components contribute meaningfully to regression performance. Under the nominal IPF condition, the baseline models achieve comparable or slightly lower errors than the CNN, reflecting their strong in-distribution performance under fixed operating conditions.

To evaluate generalization beyond narrowly defined operating conditions, the same comparison was repeated under the Intermediate condition, which spans a broader range of bulk temperatures and flow rates. As shown in Figure 9, CNN consistently outperforms the baseline models under these expanded conditions. These results indicate that while simpler models can perform well under identical training and testing conditions, CNN provides superior robustness and generalization under realistic variations in operating parameters.

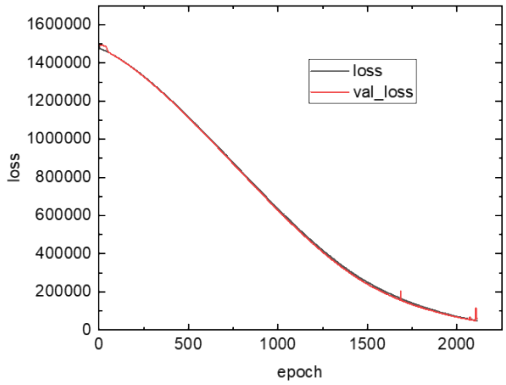

Figure 7 Training and validation learning curves for IPF condition.

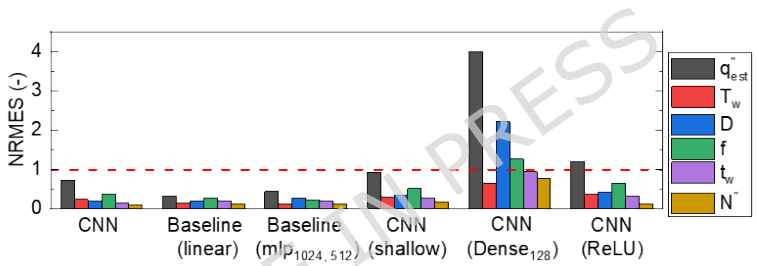

Figure 8 NRMSE at various baseline models and ablation studies (IPF condition).

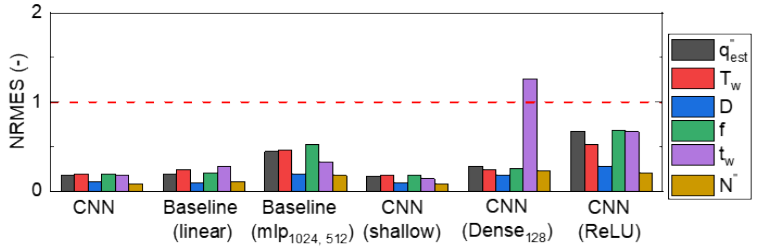

Figure 9 NRMSE at various baseline models and ablation studies (Intermediate condition).

3.1.2 Model prediction

Building upon the evaluated model, the CNN was applied to acoustic data acquired under operating conditions representative of practical deployment scenarios. The IPF condition and reduced condition were selected to examine model performance across distinct thermal and hydraulic regimes. Representative HSV and corresponding background-removed STFT spectrograms for IPF condition are shown in Figure 10 (a) to demonstrate context for the acoustic inputs and inferred parameters. Figure 10 (b) compare the boiling curves and key bubble parameters inferred from acoustic signals with reference data derived from HSV imagery and TC measurements. Error bars indicate the experimental quantified uncertainty ranges described in Section 2.1.3.

The CNN model strong predictive performance with good agreement across both conditions. Predicted boiling curves and bubble dynamics parameters remain within the experimentally observed ranges. The error bars associated with the HSV and TC data reflect both measurement and spatial variability. Notably, the relatively wide uncertainty bands primarily reflect experiment-to-experiment variability associated with localized non-uniform heat generation by the pancake induction coil, rather than from sensor or signal-processing inaccuracies. Future experiments will incorporate additional thermocouples within the test section to better quantify spatial variations in wall heat flux and improve local temperature resolution. The consistency between the acoustically inferred and visually measured parameters confirms that the CNN captured the underlying correlations between hydroacoustic features and boiling dynamics across facility-relevant operating conditions, providing a sound foundation for subsequent analyses of noise resilience and CFD integration.

Figure 10. (a) Training pair for IPF condition; (b) Comparison between the boiling parameters derived from HSV images & TCs and CNN model predictions trained on acoustic signals.

3.2 Noise interference

To evaluate the robustness of the CNN model under acoustic contamination, Gaussian white noise of varying intensity was superimposed onto the hydrophone signals. The signal-to-noise ratio (SNR), expressed in decibels (dB), was defined as:

$$SNR_{dB} = 10\log_{10}\left(\frac{P_{signal}}{P_{noise}}\right) \tag{10}$$

where P_{signal} and P_{noise} represent the power of the original and noise-added signals, respectively. To provide physical context for the noise robustness assessment, representative acoustic spectra are shown in Figure 11, including STFT spectrograms of the background signal, the raw boiling signal, the background-removed signal, and the corresponding background-removed spectrograms under representative noise interference levels. These comparisons demonstrate that the background-removal procedure effectively suppresses non-boiling broadband components while preserving boiling-related spectral features. The background-removed STFTs further illustrate how increasing noise levels progressively reduce spectral contrast. This visualization provides a physically interpretable basis for evaluating the model's robustness under acoustic interference.

Figure 12 shows the variation of NRMSE with SNR levels of 30, 20, 10, 0, and -10 dB under both the IPF and reduced conditions. Based on Eq. (9), these SNR values

correspond to noise powers that are 0.001, 0.01, 0.1, 1, and 10 times the boiling acoustic signal power, respectively. The CNN model maintained stable predictive accuracy for SNR levels down to approximately 0 dB, demonstrating strong resilience to acoustic noise. Slightly higher sensitivity was observed under the IPF condition due to the relatively weaker boiling-induced acoustic emissions at higher flow rates, which reduced the signal amplitude relative to background noise.

Figure 13 shows a comparison between the estimated heat fluxes, derived from Eq. (1), and those predicted by a CNN model across varying SNR conditions. The shaded region represents the experimental uncertainty bounds defined in Section 2.1.3. The model predictions remained well within these bounds for SNR levels of 30, 20, and 10 dB, approached the limit at 0 dB (where NRMSE ≈ 1), and deviated beyond the uncertainty range at -10 dB (NRMSE > 1). These results validate NRMSE < 1 as a robust criterion for acceptable model performance and confirm that the CNN architecture preserves predictive integrity even under substantial acoustic interference.

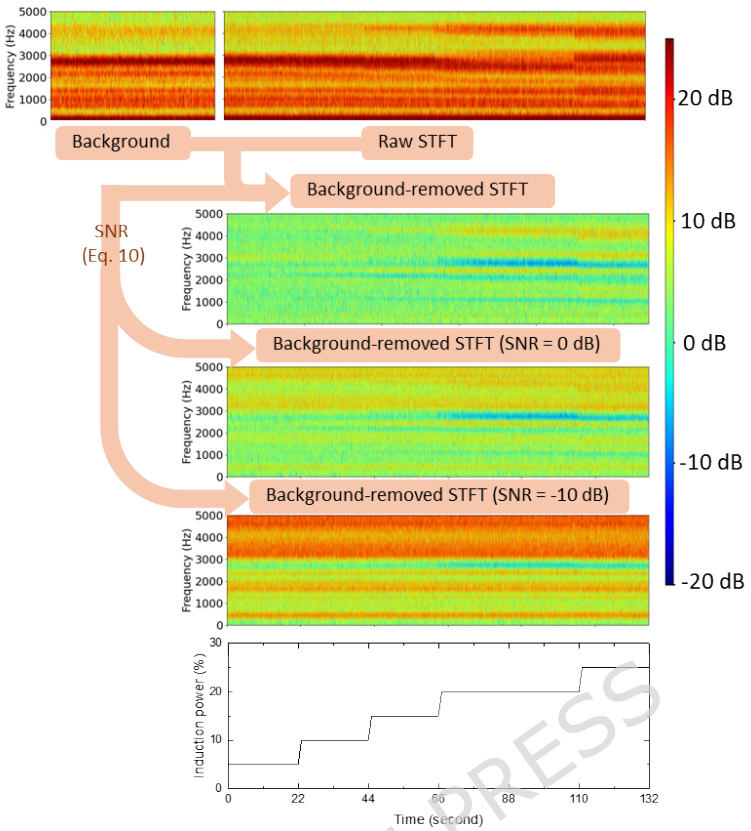

Figure 11 The background, raw, and background-removed, and noise-interfered STFT .

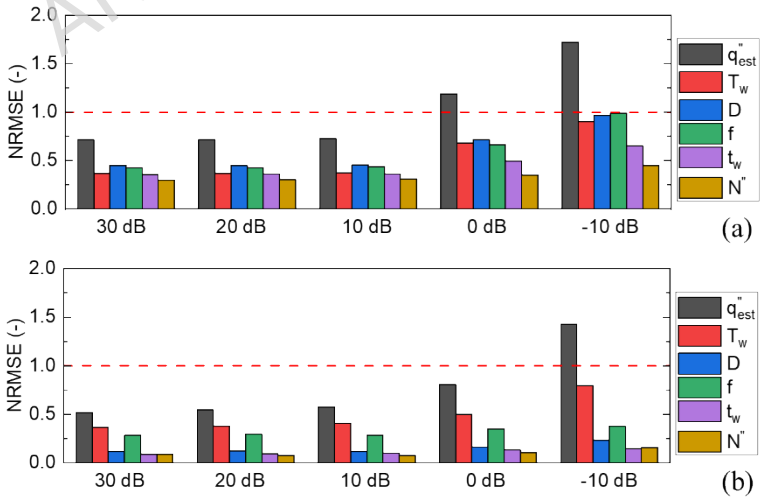

Figure 12 NRMSE at various SNR levels: (a) IPF condition; (b) reduced condition.

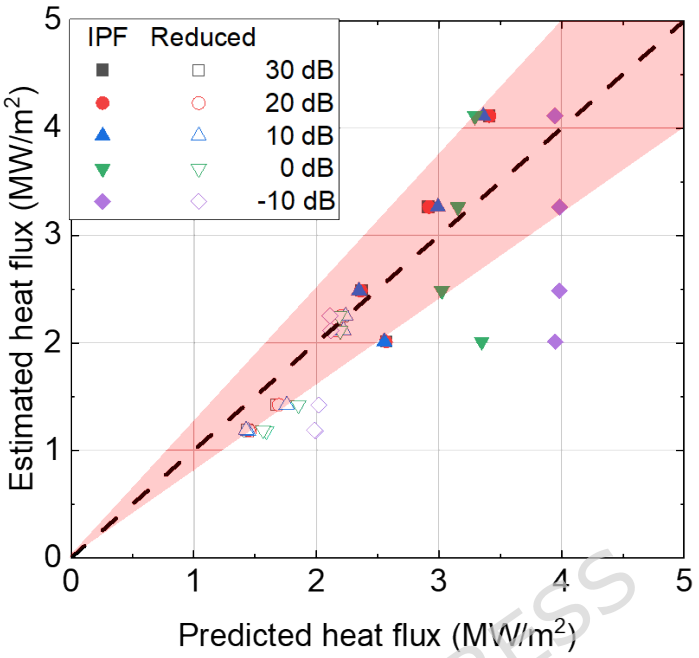

Figure 13 Estimated heat flux versus CNN-predicted heat flux under varying noise levels.

3.3 CFD performance

Building upon the previously validated acoustic predictions, the CNN-inferred boiling parameters were incorporated into the ANSYS CFX model to evaluate their capability in reproducing the subcooled flow boiling behavior and estimating CHF. The CFD simulations employed the same RPI wall-boiling framework and void fraction-based CHF criteria ($\alpha = 0.9$) that were previously validated against independent experimental CHF measurements under comparable subcooled flow boiling conditions [2]. In the present study, the CFD comparisons are therefore used to assess the physical consistency of acoustically inferred boiling parameters within

this validated framework, rather than to provide a standalone experimental validation of CHF prediction accuracy.

Because the CFD model combines multiple bubble-scale inputs within the heat-partitioning framework, uncertainties in individual predicted parameters are not linearly mapped to CHF prediction error. Figure 14 compares the predicted boiling curves using CNN-derived inputs with those obtained from HSV algorithms under both the IPF and reduced conditions. The end point of each curve indicates the predicted CHF with a void fraction of 0.9, while the shaded region denotes the ±25% uncertainty envelope associated with the reference HSV- and U-Net-based model predictions [2]. Because the heat flux and wall superheat are model outputs rather than measured quantities, and no formal uncertainty quantification was performed on the governing model parameters, error bars are not shown. Consistent with the findings in Section 3.2, the CFD results based on CNN-inferred parameters fall within these uncertainty bounds when the corresponding NRMSE values remain below unity. To further examine model resilience, Figure 15 presents the variation in CHF prediction accuracy across different noise interference levels, showing a pronounced degradation in predictive accuracy as the SNR decreased below 0 dB. For moderate noise levels (SNR ≥ 0 dB), the CNN-driven CFD framework successfully reproduced CHF behavior comparable to that obtained from visual and thermocouple-based datasets.

These results demonstrate that the acoustically inferred bubble parameters provide physically consistent inputs for CFD-based thermal modeling within the evaluated operating and noise conditions. The framework bridges acoustic diagnostics with high-fidelity simulations, paving a promising way to predictive boiling heat transfer

analysis in scenarios where conventional optical measurements are impractical or infeasible.

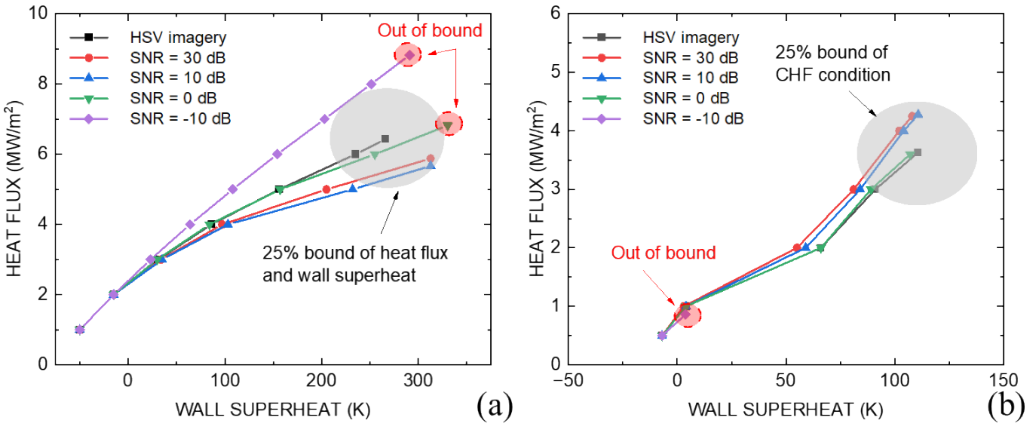

Figure 14 CFD Model-predicted subcooled flow boiling curves, using HSV-derived and CNN-inferred boiling parameters under various noise interference levels at the (a) IPF condition; (b) reduced condition.

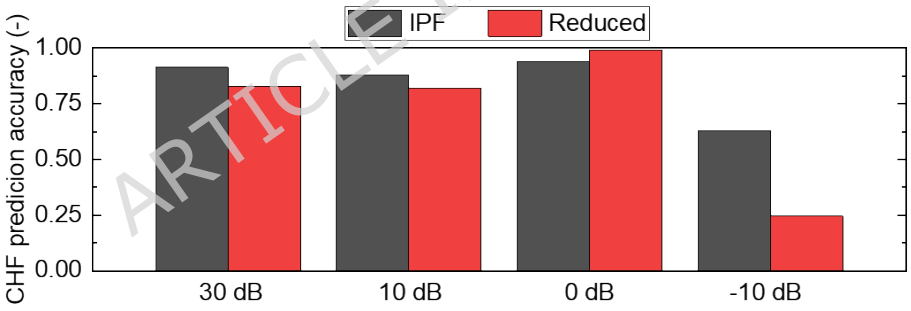

Figure 15. CHF prediction accuracy under various noise interference levels at both the IPF and reduced conditions.

3.4 Effect of Operating Parameters on Model Performance

Although background subtraction effectively suppresses non-boiling acoustic components, the intrinsic boiling dynamics remain sensitive to variations in system

boundary conditions such as bulk temperature, flow rate, and hydrophone placement. To systematically evaluate these effects, a CNN model was trained using data collected at a bulk temperature of 55°C and a flow rate of 10 GPM, encompassing 18 operating conditions with heat fluxes ranging from 1.5 to 4.3 MW/m^2, resulting in a total of 3,636 acoustic samples.

The trained model was subsequently applied to predict boiling behavior under different bulk temperatures (16, 28, and 35°C) and flow rates (1, 4, and 7 GPM) to isolate the influence of each boundary condition on predictive accuracy. Additionally, the effect of hydrophone placement was examined by comparing model performance when the sensor was located at 22.5, 39, and 55.5 inches from the test section, relative to the 6-inch reference position used for training.

As shown in Figure 16, the CNN model maintained reliable predictive capability across moderate variations in boundary conditions. The model sustained consistent accuracy for bulk temperature deviations up to approximately 20°C, flow rate reductions down to 7 GPM, and hydrophone displacements up to 22.5 inches. While larger deviations beyond these thresholds led to noticeable prediction errors, the model exhibited robust generalization and stable performance within moderate departures from tested operational envelope.

These findings indicate that the CNN framework effectively captures the coupled influence of flow and thermal boundary conditions on boiling acoustics within the tested operational envelope, supporting its applicability to facility-relevant environments. As with the noise interference results, predictive accuracy degrades progressively as operating conditions depart further from the training regime, providing a physically interpretable indication of the framework’s sensitivity to

boundary-condition variation. Future model extensions that incorporate physics-informed input features (e.g., hydrophone configuration) are expected to further enhance model adaptability and ensure reliable deployment across a broader range of operational scenarios.

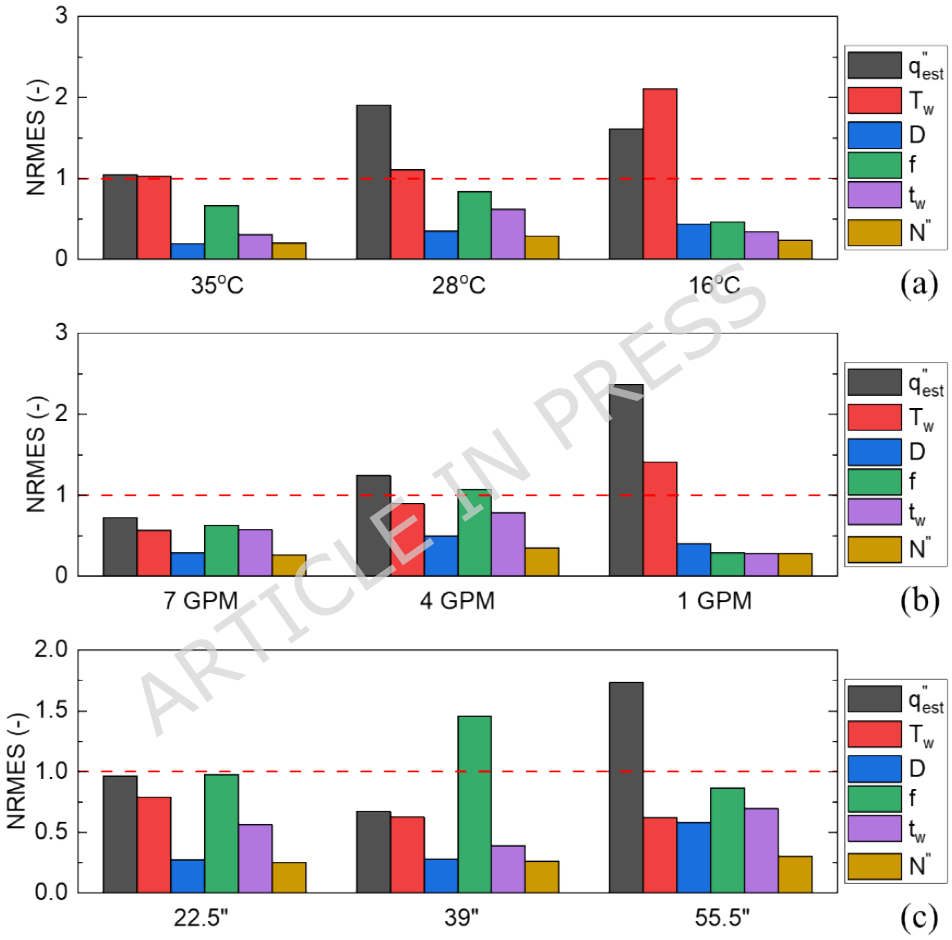

Figure 16. Model performance across variations in (a) bulk temperature; (b) flow rate; (c) hydrophone placement.

4. Conclusions and Future Work

4.1 Conclusions

This study developed and validated a non-intrusive diagnostic framework that integrates a deep learning approach based on convolutional neural networks (CNN) trained on acoustic signals. The framework predicts boiling behavior and critical heat flux (CHF) in a subcooled flow boiling system representative of the Isotope Production Facility (IPF) at Los Alamos National Laboratory. In this framework, machine-learning predictions derived from hydroacoustic signals are intended to serve as inputs to physics-based CFD or reduced-order thermal models for decision support. By transforming boiling-induced hydrophone signals into background-removed Short-Time Fourier Transform (STFT) spectrograms and processing them through a convolutional neural network (CNN), heat flux, wall superheat, and key bubble parameters – including departure diameter, departure frequency, wait time, and nucleation site density – were successfully inferred without reliance on optical diagnostics.

The CNN model achieved strong predictive performance within the evaluated operating conditions, with predicted boiling curves and bubble dynamics parameters remaining within the experimental range and uncertainty bounds of high-speed video (HSV) and thermocouple (TC) measurements. The framework demonstrated resilience to acoustic contamination within the tested SNR range, with prediction accuracy degrading in a physically interpretable manner as noise levels increased. When the acoustically inferred parameters were incorporated into the CFD framework, the resulting boiling curves and CHF estimate closely matched those obtained from visual-based datasets, confirming the physical consistency of the approach and its suitability for predictive analysis within visually restricted environment.

Furthermore, the CNN models exhibited stable performance under moderate variations in operational settings – including bulk temperature, flow rate, and hydrophone placement – indicating promising generalizability across practical operational envelopes. Collectively, these results demonstrate the feasibility and internal physical consistency of hydroacoustic-based deep learning as a pathway toward non-intrusive boiling diagnostics and predictive thermal assessment in visually restricted or radiation-limited environments.

4.2 Future Work

Future efforts will focus on improving the spatial characterization of heat flux by addressing non-uniformities introduced by the induction heating system. Additional thermocouples will be embedded in the test window to enhance local temperature and heat flux resolution. In parallel, a separate, independently instrumented boiling facility with distinct geometry and heating characteristics is being planned to generate validation data fully decoupled from the training dataset, enabling rigorous assessment of model transferability and predictive capability, including evaluation of acoustically inferred boiling parameters and CHF predictions against independent thermal benchmarks. To facilitate full-scale deployment at the IPF, upcoming studies will also expand the machine learning framework to incorporate additional metadata, allowing the model to adapt to varying experimental setups and boundary conditions. These advancements will strengthen the model's transferability from the TARDIS-β prototypical facility to the IPF cooling system, ultimately enabling a fully non-intrusive, real-time, and radiation-hardened diagnostic platform for predictive thermal safety assessment.

Acknowledgements

This work was supported by the U.S. Department of Energy (DOE) Isotope Program, managed by the Office of Science for Isotope R&D and Production. Los Alamos National Laboratory is operated by Triad National Security, LLC, for the National Nuclear Security Administration of the U.S. Department of Energy under Contract No. 89233218CNA000001.

Funding

This work was supported by the U.S. Department of Energy (DOE) Isotope Program.

Data availability

The data supporting the findings of this study are provided as Supplementary Information with this manuscript, including the raw data underlying the figures and example datasets sufficient to run the accompanying analysis and machine-learning code. The full dataset generated and analyzed during the current study is available from the first author, Dr. Huang (phhuang@lanl.gov), or the corresponding author, Dr. O'Brien (emobrien@lanl.gov) upon reasonable request and will be deposited in the Los Alamos National Laboratory Research Library and assigned a persistent DOI upon acceptance.

Reference

1. O'Brien, E. M., Baily, S. A., Birnbaum, E. R., Chapman, C., Espinoza, E. A., Faucett, J. A., ... & Woloshun, K. A. (2020). Novel design and diagnostics improvements for increased production capacity and improved reliability at the Los Alamos Isotope Production Facility. Nuclear Instruments and Methods in Physics Research Section A: Accelerators, Spectrometers, Detectors and Associated Equipment, 956, 163316.

2. Seong, J. H., Morrell, J. T., Singh, B., Woloshun, K. A., Olivas, E. R., Lance, P. K., ... & Vermeulen, C. (2023). Development of experimental and computational frameworks to predict subcooled flow boiling in the LANL Isotope Production Facility. International Journal of Heat and Mass Transfer, 203, 123836.

3. Rapisarda, D., Olmos, P., Brañas, B., Arranz, F., Iglesias, D., & Molla, J. (2015). Boiling bubbles monitoring for the protection of the LIPAc beam-dump. Fusion Engineering and Design, 96, 917-921.

4. Nishihara, H. (1974). Resonant acoustic noise spectra of nucleate coolant boiling. Journal of Nuclear Science and Technology, 11(1), 1-7.

5. Huang, P.H., Seong, J.H., Castro Aguilar, J.M., O'Brien, E.M., & Vermeulen, C., (2025, September). Acoustic Analysis to Identify Boiling Characteristics in the LANL Isotope Production Facility Cooling System. In 21st International Topical Meeting on Nuclear Reactor Thermal Hydraulics (NURETH-21).

6. Sinha, K. N. R., Ranjan, D., Raza, M. Q., Kumar, N., Kaner, S., Thakur, A., & Raj, R. (2019). In-situ acoustic detection of critical heat flux for controlling thermal runaway in boiling systems. International Journal of Heat and Mass Transfer, 138, 135-143.

7. Almadih, M. H., Almudhhi, T., Ebrahim, S., Howell, A., Garrett, G. R., Bajorek, S. M., & Cheung, F. B. (2022). Acoustic analysis of the effects of vapor-liquid interfacial morphology on pool-boiling heat transfer. Nuclear Technology, 208(8), 1290-1300.

8. Negi, A., Rishi, A. M., & Kandlikar, S. G. (2021). Effect of heat flux on bubble coalescence phenomena and sound signatures during pool boiling. Journal of Heat Transfer, 143(5), 051601.

9. Zhang, K., Yang, J., Huai, X., & Cheng, K. (2023). Highly stable subcooled flow boiling enabled by an opposed wall jet design. International Journal of Heat and Mass Transfer, 216, 124562.

10. Baek, S. H., Wu, K., Shim, H. S., Lee, D. H., Kim, J. G., & Hur, D. H. (2017). Acoustic emission monitoring of water boiling on fuel cladding surface at 1 bar and 130 bar. Measurement, 109, 18-26.

11. Kichigin, A. M., & Kesova, L. A. (1967). Relationship between the nature of acoustic oscillations and the mode of surface boiling of water in annular channels. Journal of Applied Mechanics and Technical Physics, 8(6), 54-56.

12. Schwartz, F. L., & Siler, L. G. (1965). Correlation of sound generation and heat transfer in boiling.

13. Minnaert, M. (1933). XVI. On musical air-bubbles and the sounds of running water. The London, Edinburgh, and Dublin Philosophical Magazine and Journal of Science, 16(104), 235-248.

14. Dorofeev, B. M., & Volkova, V. I. (2006). The effect of evaporation and condensation in vapor bubbles on the hydrodynamic sound generation in a subcooled boiling liquid. Acoustical Physics, 52, 173-179.

15. Bessho, Y., & Nishihara, H. (1976). Boiling acoustic emission and bubble dynamics in nucleate boiling. Journal of Nuclear Science and Technology, 13(9), 520-522.

16. Tang, J., Xie, G., Bao, J., Mo, Z., Liu, H., & Du, M. (2018). Experimental study of sound emission in subcooled pool boiling on a small heating surface. Chemical Engineering Science, 188, 179-191.

17. Ahmed, M., Habib, A., Nawal, M. M., Saikot, M. M. H., Chowdhury, M. A. H., Hoque, M. A., ... & Björnsson, P. (2023). Deep learning-based approach to R-134a bubble detection and analysis for geothermal applications. Case Studies in Thermal Engineering, 49, 103377.

18. Zhou, W., Miwa, S., Okamoto, K., Okawa, T., Tsujimura, R., & Nguyen, T. B. (2024, August). Development of the AI-Assisted Thermal Hydraulic Analysis Method for Condensing Bubbles in Vertical Subcooled Flow Boiling. In International Conference on Nuclear Engineering (Vol. 88315, p. V011T15A011). American Society of Mechanical Engineers.

19. Ravichandran, M., & Bucci, M. (2019). Online, quasi-real-time analysis of high-resolution, infrared, boiling heat transfer investigations using artificial neural networks. Applied Thermal Engineering, 163, 114357.

20. Nirapure, P., Singh, A., Rangarajan, S., & Sammakia, B. (2024, May). Image driven deep learning based compact model to predict critical heat flux in direct immersion cooling via pool boiling. In 2024 23rd IEEE Intersociety Conference on Thermal and Thermomechanical Phenomena in Electronic Systems (ITherm) (pp. 1-11). IEEE.

21. Ueki, Y., & Ara, K. (2021). Proof of concept of acoustic detection of boiling inception and state transition using deep neural network. International Communications in Heat and Mass Transfer, 129, 105675.

22. Sinha, K. N. R., Kumar, V., Kumar, N., Thakur, A., & Raj, R. (2021). Deep learning the sound of boiling for advance prediction of boiling crisis. Cell Reports Physical Science, 2(3).

23. Sinha, K. N. R., Kumar, V., Kumar, N., Thakur, A., & Raj, R. (2024). Dataset for boiling acoustic emissions: A tool for data driven boiling regime prediction. Data in Brief, 52, 109793.

24. Barathula, S., Chaitanya, S. K., & Srinivasan, K. (2023). Evaluation of machine learning models in the classification of pool boiling regimes up to critical heat flux based on boiling acoustics. International Journal of Heat and Mass Transfer, 201, 123623.

25. Zhang, K., Yang, J., Huang, C., & Huai, X. (2025). Nonintrusive identification of boiling regimes enabled by deep learning based on flow boiling acoustics. International Journal of Heat and Mass Transfer, 236, 126290.

26. Dunlap, C., Pandey, H., Weems, E., & Hu, H. (2023). Nonintrusive heat flux quantification using acoustic emissions during pool boiling. Applied Thermal Engineering, 228, 120558.

27. Lim, D., Liu, Y., & Bang, I. C. (2025). Predicting boiling heat flux, heat transfer coefficient, and regimes Non-intrusively using external acoustics and deep learning. Scientific Reports, 15(1), 22690.

28. Huang, P.H., Seong, J.H., Castro Aguilar, J.M., O'Brien, E.M., Vermeulen, C., (2025, November). Visual-Acoustic Boiling Data Driven Machine Learning for Isotope Production. In ANS Winter Meeting.

29. Ansys® CFX Fluids, Release 21.2. https://www.ansys.com/academic/ terms-and- conditions#tab1- 1.

30. Seong, J. H., Ravichandran, M., Su, G., Phillips, B., & Bucci, M. (2023). Automated bubble analysis of high-speed subcooled flow boiling images using U-net transfer learning and global optical flow. *International Journal of Multiphase Flow*, *159*, 104336.

31. Jens, W. H., & Lottes, P. A. (1951). Analysis of heat transfer, burnout, pressure drop and density date for high-pressure water (No. ANL-4627). Argonne National Lab.(ANL), Argonne, IL (United States).

32. Collier, J. G. (1994). Convective Boiling and Condensation. Oxford University Press.

33. Carey, V. P. (2020). Liquid-vapor phase-change phenomena: an introduction to the thermophysics of vaporization and condensation processes in heat transfer equipment. CRC Press.

34. Seong, J. H., Ravichandran, M., Su, G., Phillips, B., & Bucci, M. (2023). Automated bubble analysis of high-speed subcooled flow boiling images using U-net transfer learning and global optical flow. International Journal of Multiphase Flow, 159, 104336.

35. SPECIAL METALS, INCONEL® Alloy 625, UNS N06625/W.Nr. 2.4856. www.specialmetals.com . (Accessed 3 January 2023).

36. Richenderfer, A., Kossolapov, A., Seong, J. H., Saccone, G., Demarly, E., Kommajosyula, R., ... & Bucci, M. (2018). Investigation of subcooled flow boiling and CHF using high-resolution diagnostics. Experimental Thermal and Fluid Science, 99, 35-58.

37. Kenning, D. B. R. (1981). Fully-developed nucleate boiling: overlap of areas of influence and interference between bubble sites. International Journal of Heat and Mass Transfer, 24(6), 1025-1032.

38. A. GULLI, PAL, S. “Deep learning with Keras,” Packt Publishing Ltd. (2017).